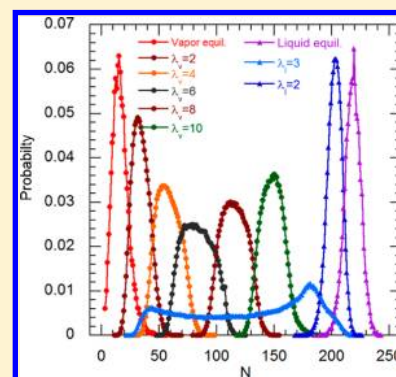


# Free Energy Barriers to Evaporation of Water in Hydrophobic Confinement

Sumit Sharma and Pablo G. Debenedetti\*

Department of Chemical and Biological Engineering, Princeton University, Princeton, New Jersey 08544, United States

**ABSTRACT:** We use umbrella sampling Monte Carlo and forward and reverse forward flux sampling (FFS) simulation techniques to compute the free energy barriers to evaporation of water confined between two hydrophobic surfaces separated by nanoscopic gaps, as a function of the gap width, at 1 bar and 298 K. The evaporation mechanism for small ( $1 \times 1 \text{ nm}^2$ ) surfaces is found to be fundamentally different from that for large ( $3 \times 3 \text{ nm}^2$ ) surfaces. In the latter case, the evaporation proceeds via the formation of a gap-spanning tubular cavity. The  $1 \times 1 \text{ nm}^2$  surfaces, in contrast, are too small to accommodate a stable vapor cavity. Accordingly, the associated free energy barriers correspond to the formation of a critical-sized cavity for sufficiently large confining surfaces, and to complete emptying of the gap region for small confining surfaces. The free energy barriers to evaporation were found to be of  $O(20kT)$  for 14 Å gaps, and to increase by approximately  $\sim 5kT$  with every 1 Å increase in the gap width. The entropy contribution to the free energy of evaporation was found to be independent of the gap width.



## I. INTRODUCTION

The behavior of water near and around apolar objects ranging from small molecules to extended hydrophobic surfaces underlies basic natural phenomena, common human activities, and novel and emerging technologies.<sup>1</sup> Examples include, respectively, the folding of globular proteins,<sup>2,3</sup> washing and cleaning, and the development of new self-cleaning<sup>4</sup> and anti-icing surfaces.<sup>5</sup> Recent work on the experimental determination of the free energy of hydrophobic hydration,<sup>6,7</sup> the computational investigation of the solubility and molecular conformation of *n*-alkanes in water,<sup>8,9</sup> and theoretical and computational studies of hydrodynamic effects in the water-mediated self-assembly of hydrophobic objects<sup>10</sup> attests to the continued interest in hydrophobicity as a subject of fundamental scientific inquiry.

At ambient temperature and pressure, water molecules form a percolating, fluctuating network of hydrogen bonds (H-bonds).<sup>11,12</sup> This self-associating nature of water governs its behavior near apolar moieties, which are incapable of forming H-bonds. Small apolar molecules exhibit a large negative entropy of hydration,<sup>13</sup> indicating a possible structural rearrangement of H-bonds between water molecules near the solute.<sup>1</sup> The quest for a fully satisfactory microscopic description of this rearrangement is an active area of research.<sup>14</sup> On the other hand, the hydration free energy of large apolar solutes (roughly  $>1 \text{ nm}$  at ambient conditions) is dominated by a large positive enthalpy change,<sup>1,15</sup> which is attributed to the inability of the water molecules close to the large solute to maintain their H-bond network. Forty years ago, Stillinger<sup>16</sup> suggested that the difficulty experienced by water molecules to preserve a H-bonded network close to a large enough hydrophobic surface can facilitate density depletion near the surface, leading to the formation of a vapor–liquid-like

interface. Subsequent theoretical work,<sup>17</sup> substantiated by numerous simulation studies, e.g., refs 18–25, has shown how such “soft” interfaces arise in practice, and highlighted the central importance of large density fluctuations near extended hydrophobic surfaces.

The above phenomena underlie the interesting and important behavior of water confined between two large hydrophobic surfaces. Thermodynamic arguments predict that, when water is confined between two macroscopic hydrophobic surfaces, the liquid state becomes metastable with respect to the vapor when the gap between the surfaces drops below distances as large as  $O(1 \mu\text{m})$ .<sup>17,26,27</sup> For nanoscopic surfaces, on the other hand, the critical distance,  $d_c$ , below which the vapor phase is stable scales as  $\sim L$ , where  $L$  is the characteristic size of the surfaces.<sup>21,22,27,28</sup> Several theoretical and computational studies have addressed this surface-induced evaporation phenomenon e.g., refs 17,20,21,29–33, which is thought play a role in the folding of globular proteins,<sup>1,2,17,34,35</sup> the opening and closing of ligand-gated ion channels,<sup>36</sup> and ligand binding to hydrophobic pockets.<sup>37</sup>

Experimental evidence shows that two macroscopic hydrophobic surfaces experience an attractive force at distances as large as 300 nm.<sup>38,39</sup> The origins of this force are still a subject of debate,<sup>40,41</sup> but cavitation to a vapor phase between the surfaces is not observed even at distances close to 20 nm.<sup>39,41–43</sup> The discrepancy between experimental observations and the thermodynamic theoretical predictions suggests that the kinetics of the evaporation process deserve careful scrutiny. Although the bulk of theoretical and computational

Received: August 22, 2012

Revised: October 15, 2012

Published: October 17, 2012

work on the subject of water evaporation in hydrophobic confinement has addressed the underlying thermodynamics, some illuminating studies have focused on the kinetics and mechanisms of this process. Leung et al.<sup>30</sup> used umbrella sampling Monte Carlo simulations along with reactive flux formalism to determine the free energy barriers to evaporation and the evaporation rate of simple point charge (SPC) water<sup>44</sup> between two infinite hydrophobic plates at different separations. Subsequently, using a lattice-gas model for water, Luzar and co-workers<sup>27,32</sup> examined the evaporation mechanism and showed that the free energy barrier to evaporation scales quadratically with  $d$ , as predicted by theoretical considerations.<sup>31</sup> Bolhuis and Chandler<sup>29</sup> studied the cavitation of the Lennard-Jones fluid confined between repulsive surfaces using transition path sampling.<sup>45</sup> Xu and Molinero<sup>33</sup> studied the thermodynamics and kinetics of liquid–vapor oscillations in a coarse-grained model of water in hydrophobic confinement. Recently,<sup>28</sup> we used forward flux sampling (FFS)<sup>46,47</sup> to compute the evaporation rate of water confined between idealized hydrophobic surfaces of lateral size  $1 \times 1 \text{ nm}^2$  and  $3 \times 3 \text{ nm}^2$ . For both surfaces, it was found that the evaporation rate decreased by roughly 2 orders of magnitude when the distance between the surfaces is increased by  $1 \text{ \AA}$ . Using a regression analysis of the evaporation rates obtained over a range of temperatures and separations between the confining surfaces,  $d$ , we estimated free energy barriers to evaporation,  $\Delta G$  of  $O(50kT)$  and observed a linear scaling of  $\Delta G$  with  $d$ .

In this paper, we directly determine the free energy barriers to water evaporation in confinement by small ( $1 \times 1 \text{ nm}^2$ ) and large ( $3 \times 3 \text{ nm}^2$ ) surfaces, using umbrella sampling Monte Carlo simulations, and forward and reverse forward flux sampling (FFS),<sup>48</sup> respectively. The analysis reveals fundamentally different evaporation mechanisms in each case. Evaporation in the presence of the larger surfaces occurs via the formation of a gap-spanning critical cavity within the metastable confined liquid. The smaller surfaces cannot accommodate a cavity, and transient expulsion of the stable liquid occurs as a result of density fluctuations. The magnitude of the computed free energy barrier for the  $3 \times 3 \text{ nm}^2$  surfaces,  $18kT$  for  $d = 14 \text{ \AA}$ , is comparable to that reported by Leung et al.<sup>30</sup> The free energy barriers scale linearly with  $d$  for both the  $1 \times 1$  and  $3 \times 3 \text{ nm}^2$  surfaces, with a slope between  $4kT$  and  $5kT$  per  $\text{\AA}$ , in agreement with the results obtained by regression of rates.<sup>28</sup> The entropic contribution to the free energy barrier is largely independent of  $d$ . Contrary to the estimates obtained by rate regression, it is not negligible.

This paper is structured as follows. Methodological details are provided in section II. Results are presented and discussed in section III. The principal conclusions are summarized in section IV, where we also suggest possible directions for future inquiry on this interesting and important topic.

## II. SYSTEM AND METHODS

**(a). System and Molecular Dynamics Simulations.** The hydrophobic surfaces, mimicking the arrangement of carbon atoms in graphene sheets, were represented by a rigid, hexagonal pattern of Lennard-Jones (LJ) atoms with a lattice constant of  $1.4 \text{ \AA}$ .<sup>28</sup> The surfaces were kept fixed, parallel to each other, separated by a distance  $d$ , and symmetrically located with respect to the center of the simulation box.<sup>28</sup> The SPC/E model of water (classic, rigid, 3-site with explicit Coulombic charges)<sup>49</sup> was used. The LJ parameters for the water–wall interaction were taken as  $\epsilon_{O-W} = 0.0289 \text{ kcal/mol}$  and  $\sigma_{O-W} =$

$3.283 \text{ \AA}$ .<sup>28</sup> The number of water molecules in the  $1.0 \times 0.9 \text{ nm}^2$  (henceforth referred to as  $1 \times 1 \text{ nm}^2$  surfaces) and  $3.2 \times 3 \text{ nm}^2$  (henceforth referred to as  $3 \times 3 \text{ nm}^2$  surfaces) simulation systems were 2329 and 4685, respectively. For the system with  $1 \times 1 \text{ nm}^2$  surfaces, the simulations were performed in a cubic simulation box. For the system with  $3 \times 3 \text{ nm}^2$  surfaces, the simulations were performed in a rectangular box of nominal dimensions  $41.5 \times 60.5 \times 60.5 \text{ \AA}^3$ . The smaller length of the simulation box was chosen in the direction normal to the plane of the hydrophobic surfaces. Care was taken to ensure that the box dimensions were large enough so that the periodic images of the surfaces did not influence the behavior of water molecules in the simulation box. The choice of a rectangular simulation box for the  $3 \times 3 \text{ nm}^2$  surfaces was made in order to decrease the number of water molecules and hence increase the computational efficiency of the simulation. The simulations were conducted in the isothermal–isobaric ( $NPT$ ) ensemble at  $298 \text{ K}$  and  $1 \text{ bar}$ . The simulation box was periodic in all directions. The MD simulations used as part of the forward and reverse FFS calculation (see below) employed a Nosé–Hoover thermostat and barostat.<sup>50,51</sup> MD simulations were performed using the Large-Scale Atomic/Molecular Massively Parallel Simulator (LAMMPS) MD package<sup>52</sup> and the long-range interactions were computed using the particle-particle-particle-mesh (PPPM) Ewald method.<sup>53</sup> The  $k$ -space vector was taken to be  $0.295 \text{ \AA}^{-1}$  and the calculations were performed on a  $25 \times 36 \times 36$  grid.

**(b). Umbrella Sampling.** The free energy profiles for the  $1 \times 1 \text{ nm}^2$  surfaces for  $d \geq 9.8 \text{ \AA}$  were generated using umbrella sampling MC simulations,<sup>54,55</sup> employing a home-grown code. Long-range electrostatic interactions were computed using the Ewald summation.<sup>53</sup> The number of  $k$ -space vectors employed was  $(2 \times 8 + 1)^3 - 1$  (equal to 4912) and the width of the Gaussian function of the screening charge was set to  $1.15 \text{ \AA}$ . In umbrella sampling MC simulation,  $NPT$  sampling is performed from a biased probability distribution:  $\omega(\varphi) \exp(-\beta(E + PV))$ , where  $\omega(\varphi)$  is the biasing function,  $E$  is the potential energy,  $P$  is the pressure,  $V$  is the instantaneous volume of the system, and  $\beta = 1/kT$ , with  $k$  Boltzmann's constant and  $T$  the temperature. The order parameter  $\varphi$  was taken to be  $N/N_{\text{liq}}$ , where  $N_{\text{liq}}$  is the mean number of confined water molecules in the liquid state for a given value of  $d$ , and  $N$  is the number of confined water molecules in a given configuration. Justification for the choice of this order parameter is provided in section III. Within an umbrella sampling window, a target value of  $\varphi$ , denoted as  $\varphi^*$ , is chosen. The functional form of  $\omega(\varphi)$  was taken to be Gaussian (i.e., a quadratic biasing potential):  $\exp(-b(\varphi^* - \varphi)^2)$ , where  $b$  is a constant. This form of the biasing function ensures that the configurational sampling favors values of  $\varphi$  close to  $\varphi^*$ . The value of  $b$  sets the width of the sampling window. Umbrella windows were selected so as to ensure sufficient overlap between the histograms of adjacent windows. The stationary distribution of  $N$ ,  $P(N)$ , was determined by applying the weighted histogram analysis method (WHAM)<sup>56</sup> to the histograms from all the windows. For  $d = 9.8 \text{ \AA}$ , eight windows were used with the following set of  $(b, \varphi^*)$  parameters:  $(0,0)$ ,  $(49.95,0.85)$ ,  $(49.95,0.7)$ ,  $(49.95,0.5)$ ,  $(49.95,0.2)$ ,  $(49.95,0)$ ,  $(99.9,0.5)$ ,  $(199.8,0.5)$ . For  $d = 11, 12, 13$ , and  $14 \text{ \AA}$ , the following set of  $(b, \varphi^*)$  parameters was chosen:  $(0,0)$ ,  $(100,0.9)$ ,  $(100,0.8)$ ,  $(100,0.7)$ ,  $(100,0.6)$ ,  $(100,0.5)$ ,  $(100,0.4)$ ,  $(100,0.3)$ ,  $(100,0.2)$ ,  $(100,0.1)$ ,  $(100,0)$ ,  $(200,0)$ . The free energy profile as a function of  $N$  is given by,  $F(N) = -kT \ln P(N)$ . The stationary distribution as a function

of some other order parameter  $\mu$  can be determined by using the following relation:<sup>53</sup>

$$P_\mu(\mu_0) = \int_N P(N) h(\mu_0|N) dN \quad (1)$$

In the above equation,  $h(\mu_0|N)$  is the fraction of configurations, for a given  $N$ , in which the value of  $\mu$  equals  $\mu_0$ .

**(c). Forward and Reverse Forward Flux Sampling.** For the  $3 \times 3 \text{ nm}^2$  surfaces, the free energy barriers were calculated by using the forward and reverse forward flux sampling (FFS) simulation technique.<sup>48</sup> We recently showed that for sufficiently large surfaces the pathway to evaporation involves the formation of a gap-spanning tubular cavity.<sup>28</sup> Therefore, a naïve umbrella sampling approach with  $N$  as the argument of the biasing potential is not in principle suitable for this case. Instead, we seek to obtain the stationary distribution  $P(N)$  by exploiting the fact that in FFS the system traverses milestones on the path between liquid and vapor basins, without being biased along any particular order parameter. In short, we compute  $P(N)$  and, via eq 1, stationary distributions of other order parameters, without biasing along  $N$ . Let the two basins of interest in the free energy landscape (e.g., confined liquid and vapor in our case) be denoted by A and B.  $P(N)$  is then written as a sum of two contributions,<sup>48</sup>

$$P(N) = \psi_A(N) + \psi_B(N) \quad (2)$$

where  $\psi_A(N)$  is the contribution to the probability density obtained from an FFS simulation going from basin A to basin B, and  $\psi_B(N)$  is the contribution to the probability density obtained from an FFS simulation going from basin B to basin A.  $\psi_A(N)$  is computed by the following relation<sup>48</sup>

$$\psi_A(N) = P_A J_A \tau_A(N, \lambda_0) \quad (3)$$

where  $P_A$  is the probability that the system is in the basin A at the given  $T$  and  $P$ .  $J_A$  is the flux of trajectories reaching the first milestone,  $\lambda_0$  in the FFS simulation from the basin A (chosen values of the order parameter used to track (not bias) the evolution of the system between the two basins are referred to as milestones<sup>28,46,47</sup>).  $\tau_A(N, \lambda_0)$  is the average time spent at the value  $N$  of the order parameter by a trajectory originating from  $\lambda_0$ .  $\tau_A(N, \lambda_0)$  is computed by the following relation:<sup>48</sup>

$$\tau_A(N, \lambda_0) = \pi_A(N, \lambda_0) + \sum_{i=1}^{n-1} \pi_A(N, \lambda_i) \prod_{j=0}^{i-1} P(\lambda_{j+1}|\lambda_j) \quad (4)$$

where  $P(\lambda_{j+1}|\lambda_j)$  is the conditional probability that a trajectory starting from milestone  $\lambda_j$  reaches milestone  $\lambda_{j+1}$  before reaching the basin A.  $\pi_A(N, \lambda_i)$  is the average time spent at the value of the order parameter  $N$  by a trajectory shot from the interface  $\lambda_i$ .  $\pi_A(N, \lambda_i)$  is given by the following relation<sup>48</sup>

$$\pi_A(N, \lambda_i) = \frac{H_N(\lambda_i) \Delta t}{\Delta N M_i} \quad (5)$$

where  $H_N(\lambda_i)$  is the histogram which stores the number of times the order parameter value  $N$  is visited by the trajectories shot from the interface  $\lambda_i$ .  $M_i$  is the total number of trajectories shot from the interface  $\lambda_i$ .  $\Delta N$  is the width of the discretized order parameter. In our case,  $N$  is the number of water molecules in the confined region, which is already a discrete variable.  $\Delta t$  is the time step for recording the current value of the order parameter of a trajectory. If  $\Delta t$  is kept constant for

the entire simulation, it can be dropped from eq 5. In determining  $H_N(\lambda_i)$ , the values of  $N$  visited by all trajectories shot from the interface  $\lambda_i$  should be included, regardless of whether they are successful in reaching the interface  $\lambda_{i+1}$  or not. Finally, the probability that the system is in basin A,  $P_A$ , can be estimated by noting that the system can be either in basin A or in basin B. Hence

$$P_A r_{AB} = P_B r_{BA} \quad (6)$$

and

$$P_A + P_B = 1 \quad (7)$$

In the above equations,  $r_{AB}$  is the rate to go from basin A to basin B, and  $r_{BA}$  is the rate to go from basin B to basin A.  $r_{AB}$  and  $r_{BA}$  are obtained from the forward and reverse FFS simulations, respectively. Using eqs 3–7,  $\psi_A(N)$  can be calculated. Analogously,  $\psi_B(N)$  can be calculated from the reverse FFS. Using the values of  $\psi_A(N)$  and  $\psi_B(N)$ ,  $P(N)$  can be determined from eq 2. The  $P(N)$  determined above is for the region in phase space between  $\lambda_0$  and  $\lambda_N$ . The histograms of  $N$  determined from MD simulations in the basins A and B can be combined with the above  $P(N)$  to determine the  $P(N)$  for the entire range of  $N$ . In order to determine the stationary distribution for a different order parameter than  $N$ , the configurations from the trajectories in the forward and backward FFS simulations can be stored and then eq 1 can be applied.

**(d). Cavity Diameter.** As discussed in ref 28 for the  $3 \times 3 \text{ nm}^2$  surfaces, the pathway to evaporation involves formation of an empty tube connecting the two surfaces. Hence, a measure of the size of this cavity may be a better choice for the order parameter than the number of confined water molecules,  $N$ . In order to determine the size of the cavity, we used the following approach. With the hydrophobic surfaces defining the direction of the  $x$ – $y$  plane, we divide this plane into a grid of cells of size  $0.2 \times 0.2 \text{ \AA}^2$ . The centers of the oxygen atoms of the confined water molecules were projected onto the  $x$ – $y$  plane. Each cell was then labeled as either “occupied” or “vacant” depending on whether the center of the cell is within a distance of  $1.583 \text{ \AA}$  from the center of an oxygen atom or not. After all the cells were labeled, a cluster analysis is performed in which vacant cells adjacent to one another in the grid are said to belong to the same cluster. The largest cluster corresponds to the largest gap-spanning cavity. The area of the largest gap-spanning cavity (since this is a 2D analysis) is determined, from which the diameter is calculated assuming that the tube is cylindrical.

### III. RESULTS AND DISCUSSION

Figure 1 shows the free energy profiles,  $\Delta G(N)/kT$ , for the  $1 \times 1 \text{ nm}^2$  surfaces for different values of  $d$ , at 298 K and 1 bar. For  $d \geq 9.8 \text{ \AA}$ ,  $\Delta G(N)/kT$  was computed from umbrella sampling MC simulations (see System and Methods section). For  $d \leq 9 \text{ \AA}$ , the free energies were obtained from long (40 ns) molecular dynamics (MD) simulations, because for these values of  $d$  both the liquid and the vapor phases in the confined region were sampled in the course of the MD simulation. The free energy profiles show that the vapor phase is metastable or unstable for  $d \geq 9 \text{ \AA}$ , and stable for  $d \leq 8 \text{ \AA}$ . This implies that the critical distance  $d_c$  below which the vapor phase is stable is less than  $9 \text{ \AA}$ . The confining hydrophobic surfaces, barely 3 water molecules across, are too small to accommodate an organized vapor cavity that can serve as a critical nucleus, in contrast to the  $3 \times 3 \text{ nm}^2$  surfaces (see below). Thus, even for  $d = 8 \text{ \AA}$ ,



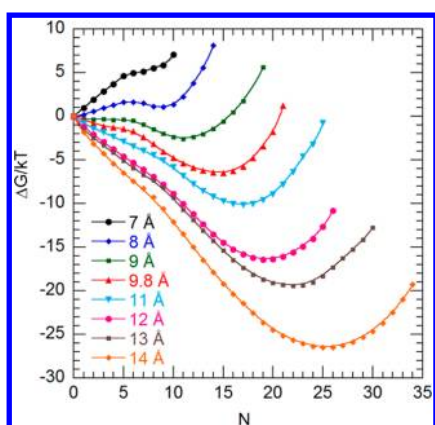


**Figure 1.** Free energy profiles as a function of the number of confined water molecules,  $N$ , for different values of  $d$ , for the  $1 \times 1 \text{ nm}^2$  surfaces. The free energy profiles for  $d \geq 9.8 \text{ Å}$  were determined using umbrella sampling Monte Carlo simulations. The free energy profiles for  $d \leq 9 \text{ Å}$  were determined from direct MD simulations.

where the liquid is unstable with respect to the vapor (see Figure 1), the transition is almost barrierless ( $\Delta G/kT = 0.5$ ). Under these conditions, the physics of the evaporation process is governed by density fluctuations, and  $N$  is the appropriate order parameter. For  $d \geq 9 \text{ Å}$ , the confined vapor is unstable and the characteristic time between fluctuation events that can lead to a transient emptying of the confined volume becomes macroscopic (e.g.,  $\sim 17 \text{ s}$  for  $d = 14 \text{ Å}$ )<sup>28</sup>.

The free energy barriers to evaporation,  $\Delta G/kT$ , are plotted in Figure 2 for different values of  $d$ . For  $d \geq 9 \text{ Å}$ , corresponding

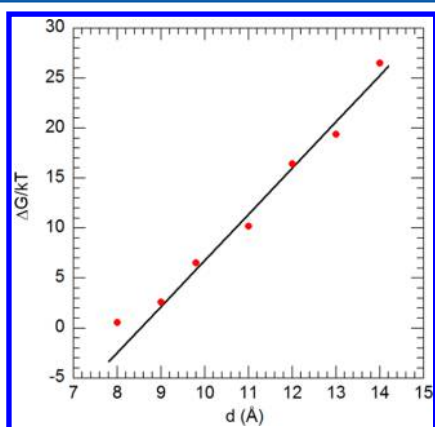


**Figure 2.** Free energy barrier,  $\Delta G/kT$ , as a function of  $d$ , for the  $1 \times 1 \text{ nm}^2$  surfaces. The values of  $\Delta G/kT$  were determined by taking the difference of the free energy for  $N = 0$  and that of the liquid phase basin, except for  $d = 8 \text{ Å}$ , for which a saddle point in the free energy profile exists at  $N = 6$ . The line is an ordinary least-squares (OLS) fit to the  $\Delta G/kT$  values for  $d = 9$  to  $14 \text{ Å}$ . The slope of the OLS fit,  $m = 4.6 \text{ kT/Å}$ .

to the case where the confined vapor is unstable (no  $N = 0$  free energy minimum in Figure 1), the free energy barrier is linear in  $d$ . This can be understood by noting that in this case there is no critical nucleus, and hence the computed curves in Figure 1 correspond to the free energy difference between the stable liquid and unstable vapor phases confined to the  $L \times L \times d$  volume between the hydrophobic surfaces, in contact with the surrounding reservoir of liquid water. This free energy difference is given by<sup>22,26,27</sup>

$$\Delta\Omega = L^2 \left( \Delta P + \frac{4\gamma}{L} \right) (d - d_c) \quad (8)$$

where  $\Delta P = P_L - P_v$  is the difference between the bulk pressure and the pressure exerted by the confined vapor (or, to an excellent approximation,<sup>26</sup> the difference between bulk and saturation pressures at the given temperature);  $\gamma$  is the vapor–liquid interfacial tension; and  $d_c$  is the critical separation between the hydrophobic surfaces, below which the confined vapor is stable. From Figure 1,  $d_c \sim 9 \text{ Å}$  (the theoretical prediction<sup>21,22,26,28</sup> is  $L/2$ , that is to say,  $5 \text{ Å}$ ). We use the symbol  $\Delta\Omega$  in eq 8 to denote the difference in grand potential between confined phases in an open system. The slope of the straight line in Figure 2,  $4.6 \text{ kT/Å}$ , is in reasonable agreement with the value predicted by eq 8,  $6.7 \text{ kT/Å}$ , with  $\Delta P \sim 1 \text{ bar}$ ,  $\gamma \sim 0.07 \text{ N/m}$  and  $L = 10 \text{ Å}$ . From the temperature dependence of the evaporation rates reported in ref 28, we obtain  $\Delta H/kT$  as a function of  $d$ ; combining this with the free energies reported here (Figure 1), we obtain  $\Delta S/k \sim 40$  and independent of  $d$  (Table 1).

**Table 1.** Thermodynamic Quantities Determined for the  $1 \times 1 \text{ nm}^2$  Surfaces<sup>a</sup>

$d \text{ (Å)}$	$\Delta G/kT$	$\ln \text{ rate (nm}^{-2} \text{ s}^{-1})$	$\ln C \text{ (nm}^{-2} \text{ s}^{-1})$	$\Delta H/kT$	$\Delta S/k$
8	0.5	23.9	24.4	39.9	39.4
9	2.6	21.2	23.8	42.6	40.0
9.8	6.5	18.0	24.5	45.7	39.2
11	10.2	13.3	23.5	51.3	41.1
12	16.4	8.2	24.7	56.0	39.6
13	19.4	4.2	23.6	60.7	41.3
14	26.5	−2.8	23.7	65.3	38.8

<sup>a</sup>The values of  $\Delta G/kT$  for  $d \geq 9.8 \text{ Å}$  were determined using umbrella sampling Monte Carlo simulations. The values of  $\Delta G/kT$  for  $d \leq 9 \text{ Å}$  were determined from direct MD simulations. The evaporation rates,  $\ln(\text{rate})$ , and the enthalpy values,  $\Delta H/kT$ , are taken from ref 28. The prefactor values,  $\ln C$ , were determined from  $\ln C = \ln(\text{rate}) + \Delta G/kT$ . The entropy values,  $\Delta S/k$ , were determined from  $\Delta S/k = \Delta H/kT - \Delta G/kT$ . The values of  $\ln C$  and  $\Delta S/k$  were found to remain approximately constant with respect to  $d$ .

Figure 3 shows the free energy profiles,  $\Delta G(N)/kT$ , for the  $3 \times 3 \text{ nm}^2$  surfaces for  $d = 12$  to  $14 \text{ Å}$  at  $T = 298 \text{ K}$  and  $P = 1 \text{ bar}$ .

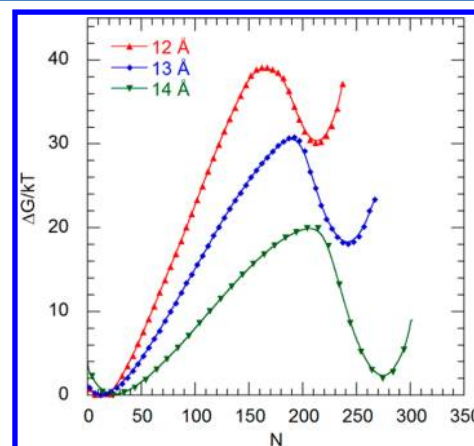


**Figure 3.** Free energy profiles as a function of the number of confined water molecules,  $N$ , for different values of  $d$ , for the  $3 \times 3 \text{ nm}^2$  surfaces. The free energy profiles were determined by doing forward and reverse FFS simulations. For all  $d$ , the vapor phase is the stable phase.

The  $\Delta G(N)/kT$  profiles were calculated from forward and reverse forward flux sampling simulations<sup>48</sup> to get the stationary distribution of the number of confined water molecules,  $N$ , for each  $d$  (see Systems and Methods section). The magnitude of the computed free energy barrier for  $d = 14$  Å is  $18kT$ , which is comparable to that reported by Leung et al.<sup>30</sup> For the values of  $d$  studied, the vapor phase is more stable than the liquid phase. Hence, for the  $3 \times 3$  nm<sup>2</sup> surfaces, the evaporation mechanism is an activated, nucleation process, as can be seen from the barrier separating the metastable (liquid) and vapor basins. For  $d = 14$  Å, the free energy of the liquid phase is only  $\sim 2kT$  higher than the vapor phase implying we are quite close to the value of the critical distance,  $d_c$ , for which the theoretical prediction is  $d_c \sim L/2 = 15$  Å.<sup>22,26,28</sup> Note the improved agreement between the theoretical prediction for  $d_c$  and the simulation results for the case of the  $3 \times 3$  nm<sup>2</sup> surfaces compared to the corresponding  $1 \times 1$  nm<sup>2</sup> case. This reflects the gradual improvement of macroscopic predictions as the size of the confining surfaces increases.

As shown in our recent study,<sup>28</sup> evaporation from the confined space between the  $3 \times 3$  nm<sup>2</sup> surfaces occurs via formation of a gap-spanning tubular cavity. The free energy cost of forming a cylindrical vapor tube of radius  $r$  is given by<sup>22,26,28</sup>

$$\begin{aligned}\Delta\Omega &= 2\pi(d\gamma + 2\lambda)r - \pi r^2[-2\gamma \cos\theta - d\Delta P] \\ &\approx 2\pi(d\gamma + 2\lambda)r + 2\pi r^2\gamma \cos\theta\end{aligned}\quad (9)$$

Equation 9 incorporates the effect of line tension,  $\lambda$ , which, as we showed in earlier work, can be important.<sup>28</sup> In the above equations,  $\theta$  is the contact angle of water on the hydrophobic surface, and the other symbols have already been explained. The final form of eq 9 follows from the fact that  $\gamma \gg d\Delta P$  under the conditions of interest here ( $\gamma \sim 0.07$  N/m,  $d \sim 1$  nm,  $\Delta P = 1$  bar).

The radius of the critical gap-spanning tube (that is to say the gap-spanning tube corresponding to the top of the free energy curves in Figure 3) is given by

$$r^* = \frac{-1}{\cos\theta} \left( \frac{d}{2} + \frac{\lambda}{\gamma} \right) \quad (10)$$

where use has been made of the above-mentioned inequality,  $\gamma \gg d\Delta P$ . Substituting for  $r^*$  in 9, we obtain the corresponding free energy barrier

$$\Delta\Omega = \frac{-\pi}{\cos\theta} \left[ \frac{\gamma d^2}{2} + 2\lambda d + \frac{2\lambda^2}{\gamma} \right] \quad (11)$$

The remarkably different free energy profiles for the  $1 \times 1$  nm<sup>2</sup> and the  $3 \times 3$  nm<sup>2</sup> surfaces for the same value of  $d$  can be understood<sup>22</sup> by analyzing eq 9.  $\Delta\Omega$  is a concave downward parabola in  $r$ , which has a maximum at  $r = r^*$  given by eq 10 and two roots, at  $r = 0$  and  $r = 2r^*$ . The free energy difference between the vapor and the liquid states in the confined region can be rationalized by considering the case  $r = L$  in eq 9. For a given value of  $d$ , if  $L < r^*$ , there is no maximum as  $r$  is increased from 0 to  $L$ . The liquid phase is the stable phase as  $\Delta\Omega$  is positive for  $r = L$ . The free energy profiles for the  $1 \times 1$  nm<sup>2</sup> surfaces (Figure 1) are a manifestation of this scenario. If  $2r^* > L > r^*$ , as one goes from  $r = 0$  to  $r = L$ , a maximum is present at  $r = r^*$ , and the liquid phase is more stable than the vapor phase, as  $\Delta\Omega$  is positive for  $r = L$ . If  $L > 2r^*$ , an extremum is present at  $r = r^*$ , and the vapor phase is more stable than the liquid phase,

because  $\Delta\Omega$  is negative for  $r = L$ . This is the case for the  $3 \times 3$  nm<sup>2</sup> surfaces, as illustrated in Figure 3.

We now investigate whether a measure of the size of the vapor tube could be a better order parameter than  $N$  to describe the progress of the liquid-to-vapor transition for the  $3 \times 3$  nm<sup>2</sup> surfaces. Figure 4 shows the free energy profiles,

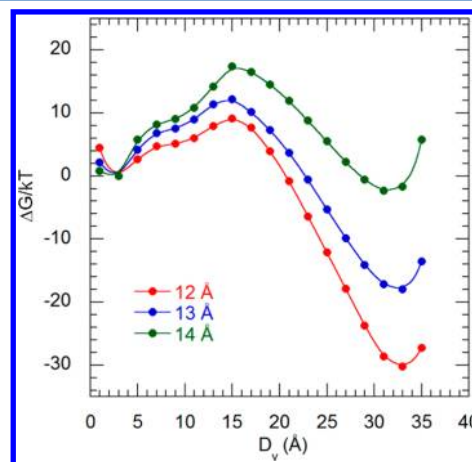


**Figure 4.** Free energy profiles for different values of  $d$  as a function of the diameter of the vapor cavity,  $D_v$ , for the  $3 \times 3$  nm<sup>2</sup> surfaces. Since  $D_v$  is a continuous variable, the values of  $D_v$  were binned in histograms of width 2 Å. The lines are guides to the eye.

$\Delta G(D_v)/kT$ , when the diameter of the largest vapor cavity,  $D_v$ , is used as the order parameter (see System and Methods section). Equation 1 was used to calculate these free energy profiles. The critical vapor diameter is estimated to be  $\sim 15$  Å for the three values of  $d$  investigated here. Table 2 lists the

**Table 2. Thermodynamic Quantities Determined for the  $3 \times 3$  nm<sup>2</sup> Surfaces<sup>a</sup>**

$d$ (Å)	$\Delta G(N)/kT$	$\ln \text{rate (nm}^{-2} \text{ s}^{-1})$	$\ln C \text{ (nm}^{-2} \text{ s}^{-1})$	$\Delta H/kT$	$\Delta S/k$	$\Delta G(D_v)/kT$
12	9.0	13.8	22.8	63.4	54.4	9.3
13	12.8	10.2	23.0	67.1	54.3	13.0
14	18.0	3.04	21.04	74.2	56.2	18.0

<sup>a</sup>The values of the free energy barrier using  $N$  as the reaction coordinate,  $\Delta G(N)/kT$ , were determined by doing forward and reverse FFS simulations in  $N$ . The values of the free energy barrier using the diameter of the vapor cavity,  $D_v$ , as the reaction coordinate,  $\Delta G(D_v)/kT$ , were determined by applying eq 1 in the text. The evaporation rates,  $\ln(\text{rate})$ , and the enthalpy values  $\Delta H/kT$  are from ref 28. The prefactor values,  $\ln C$ , were determined from  $\ln C = \ln(\text{rate}) + \Delta G(N)/kT$ . The entropy values,  $\Delta S/k$ , were determined from  $\Delta S/k = \Delta H/kT - \Delta G(N)/kT$ . The values of  $\ln C$  and  $\Delta S/k$  were found to remain approximately constant with respect to  $d$ . The values of  $\Delta G(N)/kT$  and  $\Delta G(D_v)/kT$  for all values of  $d$  were found to be close to each other.

values of the free energy barriers estimated by using  $N$  and  $D_v$  as the order parameters. It can be seen that the barriers are very similar. Using the evaporation rate data from ref 28 and the Arrhenius expression  $j = C \exp(-\Delta G/kT)$ , we obtain a prefactor  $C \sim 4.8 \times 10^9$  nm<sup>-2</sup> s<sup>-1</sup>, which corresponds to an attempt frequency of  $\sim 20$  ps. As was the case for the  $1 \times 1$  nm<sup>2</sup> surfaces, the entropy barrier,  $\Delta S/k$ , shows no significant dependence on the gap,  $d$ .  $\Delta S/k$  was obtained from the free energies calculated in this work and the enthalpy barriers

obtained in ref 28. From the temperature dependence of the evaporation rates, we obtained in ref 28 a linear dependence of  $\Delta H/kT$  on  $d$  for the  $3 \times 3 \text{ nm}^2$  surfaces. A  $d$ -independent  $\Delta S/k$  implies that the free energy barriers to evaporation are also approximately linear in  $d$  (see, e.g., Figure 3 in ref 28).

Figure 5 shows a plot of the probability of reaching the vapor phase for 570 configurations close to the transition region as a

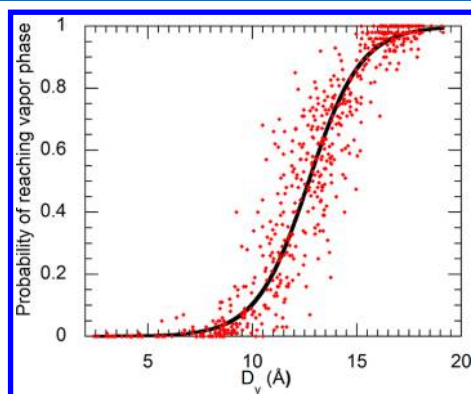


**Figure 5.** Probability of reaching the vapor phase for 570 different configurations as a function of the diameter of the largest gap-spanning cavity,  $D_v$ , for the  $3 \times 3 \text{ nm}^2$  surfaces for  $d = 13 \text{ Å}$ . The probability to reach the vapor phase was determined by shooting 100 trajectories with randomized velocities for each configuration and counting the number of trajectories that reached the vapor phase. The line is a sigmoidal fit to the data.

function of  $D_v$ , for  $d = 13 \text{ Å}$ . These probabilities were obtained by launching 100 MD simulations from each configuration stored at FFS interfaces with  $N$  varying from 174 to 210, after randomizing the velocities. The plot shows considerable scatter, implying that  $D_v$  does not fully capture the characteristics of the transition state ensemble. A general trend whereby a larger  $D_v$  corresponds to a larger probability of reaching the vapor phase is clearly seen. We also note that a probability of 0.5 is observed for configurations with  $D_v$  ranging from 11 to 14 Å, different from the critical vapor diameter predicted in Figure 4. Other candidates for the order parameter were tested, such as the volume of the tubular cavity, the size of the largest cylinder that can be inserted in the tubular cavity without overlapping with any water molecules, the smaller principal eigenvalue of the radius of gyration of the tube's circumference, and the product of the small and the large eigenvalues (a measure of the area of the vapor tube assuming it to be elliptical in 2D). None of the parameters gave a more satisfactory fit than  $D_v$ .

#### IV. CONCLUSION

In this work we have computed the free energy barriers to the evaporation of water confined by nanoscopic slitlike hydrophobic surfaces. When the size  $L$  of the confining surfaces is too small to accommodate a cavity (a situation represented here by the  $1 \times 1 \text{ nm}^2$  surfaces), the vapor is unstable or metastable with respect to the liquid except at very small values of the gap  $d$  between surfaces (here  $d < 9 \text{ Å}$ ). The computed barriers correspond to the difference between the free energies of the vapor and liquid phases occupying the entire confined space, and the previously computed evaporation kinetics<sup>28</sup> give the frequency with which density fluctuations can cause the transient emptying of the liquid-filled space. When the size of the confining surfaces is large enough to accommodate a cavity

(a situation represented here by the  $3 \times 3 \text{ nm}^2$  surfaces), the liquid is metastable with respect to the vapor phase, and evaporation proceeds by nucleation, with a gap-spanning tubular cavity acting as a critical nucleus. The computed free energy barriers yield the reversible work needed to form such a critical nucleus.

The computed free energy barriers exhibit an approximately linear dependence on gap size (see Figure 2). For the  $1 \times 1 \text{ nm}^2$  surfaces, this follows directly from the fact that the relevant free energy change corresponds to the difference between a vapor- and a liquid-filled cavity, as given by eq 8. For the  $3 \times 3 \text{ nm}^2$  surfaces, on the other hand, the approximate linearity (see Figure 3 in ref 28) suggests that line tension may be important under the conditions investigated.<sup>28</sup> Calculations spanning a broader range in the gap  $d$  between confining surfaces are needed to ascertain more accurately the importance of line tension. The free energy barriers increase by ca.  $5kT$  for every 1 Å increase in the gap,  $d$ , implying a corresponding drop in the evaporation rate of some 2 orders of magnitude per Å. When the free energies computed herein are combined with the previously calculated enthalpy barriers,<sup>28</sup> we obtain entropic contributions to the free energy barrier that are largely independent of the gap over the range of conditions investigated here. Contrary to the entropy barriers estimated by regression of rates as a function of temperature and gap size,<sup>28</sup> the entropy barriers computed here are not negligible (e.g.,  $\Delta G/kT = 12.8$ ,  $\Delta H/kT = 67.1$ ,  $\Delta S/k = 54.3$  for  $d = 12 \text{ Å}$  and  $3 \times 3 \text{ nm}^2$  surfaces; see Table 2). The regression technique involved extrapolation of computed rates to the  $1/T \rightarrow 0$  and  $d \rightarrow 0$  limits.<sup>28</sup> The breakdown of linear behavior shown in Figure 2 for small  $d$ , not taken into consideration in ref 28, points to a possible cause of the discrepancy between regressed and computed quantities. We are currently investigating this interesting question in more detail.

While the evaporation process whereby water is expelled from the region between the larger,  $3 \times 3 \text{ nm}^2$  surfaces, is an activated event that conforms to the basic picture of classical nucleation theory, the precise identification of a suitable reaction coordinate for this event requires further investigation. Here, we have used both the diameter of the largest cavity (assumed to be cylindrical) and the number of confined water molecules. While the resulting free energy barriers corresponding to these order parameters are comparable, neither one is a fully satisfactory candidate. As suggested by the scatter in the probability of reaching the vapor basin (Figure 5) and by the apparent insensitivity of the diameter of the critical cavity to the gap size (Figure 4), a more refined geometric characterization of the critical cavity is required, and we are currently pursuing this line of inquiry by analyzing the size and the shapes of the vapor cavities by using Voronoi<sup>57,58</sup> and instantaneous surfaces techniques.<sup>59</sup> As for the number of confined water molecules, even if the calculation did not involve biasing along this coordinate, it is clear that this is simply too coarse a choice of variable to describe the underlying process of cavity formation.<sup>28</sup>

The calculations performed herein involve different methodologies for the small and large surface cases. In the former case, since the underlying physics is simply that of density fluctuations, umbrella sampling along a reaction coordinate given by the number of confined water molecules is both appropriate and convenient. In the latter case, biasing along this same reaction coordinate is clearly incorrect, and the stationary distribution of the number of confined water molecules was



reconstructed by combining forward and reverse FFS calculations.<sup>48</sup> Clearly, the physical situation considered here is sufficiently rich as to warrant further consideration, with an eye toward developing additional computational methodologies for the calculation of both rates and barriers.

Several directions for future inquiry, in addition to those alluded to above, deserve mentioning. These include the scaling of nucleation rates with  $1/L$  and the approach to the  $1/L \rightarrow 0$  limit; the scaling of rates and barriers with water–wall attractions; the influence of ambient pressure on evaporation rates and barriers; and the behavior of nucleation rates and barriers in the presence of chemically heterogeneous and geometrically complex surfaces. Finally, we mention the important and interesting question of hydrophobic collapse kinetics, whereby evaporation is coupled to the motion of the confining surfaces. Elucidating the principles governing the coupling between intrinsic evaporation kinetics<sup>28</sup> and both the reversible and dissipative<sup>10</sup> aspects of the motion of the confining surfaces is important for a predictive and quantitative understanding of the kinetics of self-assembly processes. Our previous results<sup>28</sup> show a strong dependence of the evaporation rate of confined water on the gap  $d$  between surfaces: a 1 Å increase in the gap typically causes the evaporation rate to decrease by 2 orders of magnitude. This suggests that the time scales associated with the evaporation of confined water in biological systems may in some cases become comparable to the characteristic times relevant to large-scale conformational change (e.g., protein folding). However, this possible coupling between evaporation and self-assembly needs careful experimental scrutiny.

## AUTHOR INFORMATION

### Corresponding Author

\*E-mail: pdebene@princeton.edu. Phone: (609) 258-5480.

### Notes

The authors declare no competing financial interest.

## ACKNOWLEDGMENTS

We are grateful to Amish Patel, Shekhar Garde, and Alenka Luzar for helpful discussions. The financial support of Unilever UK Central Resources and the National Science Foundation (Grants CHE-0908265 and CHE-1213343 to P.G.D.) is gratefully acknowledged. Computations were performed at the Terascale Infrastructure for Groundbreaking Research in Engineering and Science (TIGRESS) at Princeton University.

## REFERENCES

- (1) Chandler, D. *Nature* **2005**, 437 (7059), 640–647.
- (2) Kauzmann, W. *Adv. Protein Chem.* **1959**, 14, 1–63.
- (3) Rose, G. D.; Roy, S. *Proc. Natl. Acad. Sci. U.S.A.* **1980**, 77 (8), 4643–4647.
- (4) Blosssey, R. *Nat. Mater.* **2003**, 2 (5), 301–306.
- (5) Cao, L. L.; Jones, A. K.; Sikka, V. K.; Wu, J. Z.; Gao, D. *Langmuir* **2009**, 25, 12444–12448.
- (6) Li, I. T. S.; Walker, G. C. *Proc. Natl. Acad. Sci. U.S.A.* **2011**, 108 (40), 16527–16532.
- (7) Garde, S.; Patel, A. J. *Proc. Natl. Acad. Sci. U.S.A.* **2011**, 108 (40), 16491–16492.
- (8) Ferguson, A. L.; Debenedetti, P. G.; Panagiotopoulos, A. Z. *J. Phys. Chem. B* **2009**, 113, 6405–6414.
- (9) Ferguson, A. L.; Panagiotopoulos, A. Z.; Kevrekidis, I. G.; Debenedetti, P. G. *Proc. Natl. Acad. Sci. U.S.A.* **2010**, 107 (31), 13597–13602.
- (10) Morrone, J. A.; Li, J.; Berne, B. J. *J. Phys. Chem. B* **2012**, 116, 378–389.
- (11) Eaves, J. D.; Loparo, J. J.; Fecko, C. J.; Roberts, S. T.; Tokmakoff, A.; Geissler, P. L. *Proc. Natl. Acad. Sci. U.S.A.* **2005**, 102 (37), 13019–13022.
- (12) Stanley, H. E.; Teixeira, J. *J. Chem. Phys.* **1980**, 73 (7), 3404–3422.
- (13) Blokzijl, W.; Engberts, J. B. F. N. *Angew. Chem.* **1993**, 32 (11), 1545–1579.
- (14) Ball, P. *Nature* **2003**, 423 (6935), 25–26.
- (15) Rajamani, S.; Truskett, T. M.; Garde, S. *Proc. Natl. Acad. Sci. U.S.A.* **2005**, 102 (27), 9475–9480.
- (16) Stillinger, F. H. *J. Solution Chem.* **1973**, 2 (2–3), 141–158.
- (17) Lum, K.; Chandler, D.; Weeks, J. D. *J. Phys. Chem. B* **1999**, 103, 4570–4577.
- (18) Godawat, R.; Jamadagni, S. N.; Garde, S. *Proc. Natl. Acad. Sci. U.S.A.* **2009**, 106 (36), 15119–15124.
- (19) Patel, A. J.; Varilly, P.; Chandler, D. *J. Phys. Chem. B* **2010**, 114, 1632–1637.
- (20) Pangali, C.; Rao, M.; Berne, B. J. *J. Chem. Phys.* **1979**, 71 (7), 2975–2981.
- (21) Wallqvist, A.; Berne, B. J. *J. Phys. Chem.* **1995**, 99, 2893–2899.
- (22) Huang, X.; Margulis, C. J.; Berne, B. J. *Proc. Natl. Acad. Sci. U.S.A.* **2003**, 100 (21), 11953–11958.
- (23) Huang, X.; Margulis, C. J.; Berne, B. J. *J. Phys. Chem. B* **2003**, 107, 11742–11748.
- (24) Liu, P.; Huang, X. H.; Zhou, R. H.; Berne, B. J. *Nature* **2005**, 437 (7055), 159–162.
- (25) Patel, A. J.; Varilly, P.; Jamadagni, S. N.; Acharya, H.; Garde, S.; Chandler, D. *Proc. Natl. Acad. Sci. U.S.A.* **2011**, 108 (43), 17678–17683.
- (26) Cerdeirina, C. A.; Debenedetti, P. G.; Rossky, P. J.; Giovambattista, N. *J. Phys. Chem. Lett.* **2011**, 2, 1000–1003.
- (27) Lum, K.; Luzar, A. *Phys. Rev. E* **1997**, 56 (6), R6283–R6286.
- (28) Sharma, S.; Debenedetti, P. G. *Proc. Natl. Acad. Sci. U.S.A.* **2012**, 109 (12), 4365–4370.
- (29) Bolhuis, P. G.; Chandler, D. *J. Chem. Phys.* **2000**, 113 (18), 8154–8160.
- (30) Leung, K.; Luzar, A.; Bratko, D. *Phys. Rev. Lett.* **2003**, 90 (6), 065502.
- (31) Lum, K.; Chandler, D. *Int. J. Thermophys.* **1998**, 19 (3), 845–855.
- (32) Luzar, A. *J. Phys. Chem. B* **2004**, 108, 19859–19866.
- (33) Xu, L. M.; Molinero, V. *J. Phys. Chem. B* **2010**, 114, 7320–7328.
- (34) Tanford, C. *J. Am. Chem. Soc.* **1962**, 84, 4240.
- (35) Zhou, R. H.; Huang, X. H.; Margulis, C. J.; Berne, B. J. *Science* **2004**, 305 (5690), 1605–1609.
- (36) Zhu, F. Q.; Hummer, G. *Proc. Natl. Acad. Sci. U.S.A.* **2010**, 107 (46), 19814–19819.
- (37) Modis, Y.; Ogata, S.; Clements, D.; Harrison, S. C. *Proc. Natl. Acad. Sci. U.S.A.* **2003**, 100 (12), 6986–6991.
- (38) Israelachvili, J.; Pashley, R. *Nature* **1982**, 300 (5890), 341–342.
- (39) Rabinovich, Y. I.; Derjaguin, B. V.; Churaev, N. V. *Adv. Colloid Interface Sci.* **1982**, 16, 63–78.
- (40) Mastropietro, D. J.; Ducker, W. A. *Phys. Rev. Lett.* **2012**, 108 (10), 106101.
- (41) Wang, J. L.; Yoon, R. H.; Eriksson, J. C. *J. Colloid Interface Sci.* **2011**, 364 (1), 257–263.
- (42) Parker, J. L.; Claesson, P. M.; Attard, P. *J. Phys. Chem.* **1994**, 98, 8468–8480.
- (43) Meyer, E. E.; Lin, Q.; Israelachvili, J. N. *Langmuir* **2005**, 21, 256–259.
- (44) Berendsen, H. J. C.; Postma, J. P. M.; van Gunsteren, W. F.; Hermans, J. *Intermolecular forces*; D. Reidel Publishing Co.: Dordrecht, The Netherlands, 1981; pp 331–342.
- (45) Bolhuis, P. G.; Dellago, C.; Geissler, P. L.; Chandler, D. *J. Phys.: Condens. Matter* **2000**, 12 (8A), A147–A152.
- (46) Allen, R. J.; Frenkel, D.; ten Wolde, P. R. *J. Chem. Phys.* **2006**, 124 (2), 024102.

- (47) Allen, R. J.; Frenkel, D.; ten Wolde, P. R. *J. Chem. Phys.* **2006**, *124* (19), 194111.
- (48) Valeriani, C.; Allen, R. J.; Morelli, M. J.; Frenkel, D.; ten Wolde, P. R. *J. Chem. Phys.* **2007**, *127* (11), 114109.
- (49) Berendsen, H. J. C.; Grigera, J. R.; Straatsma, T. P. *J. Phys. Chem.* **1987**, *91*, 6269–6271.
- (50) Hoover, W. G. *Phys. Rev. A* **1985**, *31* (3), 1695–1697.
- (51) Hoover, W. G. *Phys. Rev. A* **1986**, *34* (3), 2499–2500.
- (52) Plimpton, S. J. *Comput. Phys.* **1995**, *117* (1), 1–19.
- (53) Allen, M. P.; Tildesley, D. J. *Computer Simulation of Liquids*; Oxford University Press Inc.: New York, 1987; pp 100–123.
- (54) Torrie, G. M.; Valleau, J. P. *Chem. Phys. Lett.* **1974**, *28* (4), 578–581.
- (55) Shen, V. K.; Debenedetti, P. G. *J. Chem. Phys.* **1999**, *111* (8), 3581–3589.
- (56) Kumar, S.; Bouzida, D.; Swendsen, R. H.; Kollman, P. A.; Rosenberg, J. M. *J. Comput. Chem.* **1992**, *13* (8), 1011–1021.
- (57) Ruocco, G.; Sampoli, M.; Vallauri, R. *J. Chem. Phys.* **1992**, *96*, 6167–6176.
- (58) Huang, X.; Margulis, C. J.; Li, Y.; Berne, B. J. *J. Am. Chem. Soc.* **2005**, *127*, 17842–17851.
- (59) Willard, A. P.; Chandler, D. *J. Phys. Chem. B* **2010**, *114*, 1954–1958.